Physiological Measurement

IPEM
Institute of Physics and
Engineering in Medicine

CrossMark

PAPER

Sensitivity volume as figure-of-merit for maximizing data importance in electrical impedance tomography

Claire C Onsager[1] , **Chulin Wang**[1] , **Charles Costakis**[1], **Can C Aygen**[1] , **Lauren Lang**[1] ,
Suzan van der Lee[2] and **Matthew A Grayson**[1]

[1] Department of Electrical and Computer Engineering, Northwestern University, Evanston, IL, United States of America
[2] Department of Earth and Planetary Sciences, Northwestern University, Evanston IL, United States of America

E-mail: m-grayson@northwestern.edu

Abstract

Objective. Electrical impedance tomography (EIT) is a noninvasive imaging method whereby electrical measurements on the periphery of a heterogeneous conductor are inverted to map its internal conductivity. The EIT method proposed here aims to improve computational speed and noise tolerance by introducing sensitivity volume as a figure-of-merit for comparing EIT measurement protocols. *Approach.* Each measurement is shown to correspond to a sensitivity vector in model space, such that the set of measurements, in turn, corresponds to a set of vectors that subtend a sensitivity volume in model space. A maximal sensitivity volume identifies the measurement protocol with the greatest sensitivity and greatest mutual orthogonality. A distinguishability criterion is generalized to quantify the increased noise tolerance of high sensitivity measurements. *Main result.* The sensitivity volume method allows the model space dimension to be minimized to match that of the data space, and the data importance to be increased within an expanded space of measurements defined by an increased number of contacts. *Significance.* The reduction in model space dimension is shown to increase *computational efficiency*, accelerating tomographic inversion by several orders of magnitude, while the enhanced sensitivity *tolerates higher noise* levels up to several orders of magnitude larger than standard methods.

1. Introduction

Electrical impedance tomography (EIT) of conducting volumes holds great promise, particularly in the field of medicine as an alternative or a complement to x-ray computed tomography (CT), magnetic resonance imaging (MRI), and sonograms, with further applications in sensors (Liu *et al* 2020), engineering (Jordana *et al* 2001, Tapp *et al* 2003), and geoscience (Ducut *et al* 2022). Although its images may have lower resolution than some of these competing methods, the disadvantage of EIT's diffuse nature can be compensated by the advantages of being radiation-free, easily portable, wearable for extended periods, and low-cost. Two longstanding challenges have prevented wider adoption of EIT in potential applications. First, the computational time of existing algorithms increases exponentially with the dimension of the model space (Boyle *et al* 2012). The ill-posed nature of the inverse problem under standard algorithms employs a dense mesh of upwards of 10 000 model elements, necessitating computationally costly regularization with no benefit in resolution. The second challenge is that present-day EIT relies on data spaces which include low sensitivity measurements whose data are vulnerable to experimental noise. Error in these low sensitivity measurements will impair the fidelity of the inverse problem, further reducing the resolution of the inverted model. In this work, we reframe the EIT problem by introducing a sensitivity volume figure-of-merit into a modified EIT method in order to create a model space of reduced dimensionality that achieves rapid computational refresh rates, while acquiring only

data of *high importance*, thereby accelerating data collection and enhancing robustness against experimental noise.

The remainder of this paper is structured as follows. Section 2 reviews standard EIT concepts in anticipation of section 3, which summarizes the overall strategy of the sensitivity volume method. Section 4 demonstrates this sensitivity volume method with example simulations resulting in orders-of-magnitude accelerated computational time or orders-of-magnitude enhanced noise tolerance, compared to state-of-the-art EIT inverse solvers. Finally, for comparison section 5 contextualizes other strategies in the literature for optimization of the EIT inverse problem.

2. Standard EIT

The essential components of an EIT method are reviewed here with notation drawn from Tarantola (2005). The description of the EIT problem begins with a model $\mathbf{m}$ representing a conductivity map of a sample. The generalized forward EIT problem

$$\mathbf{d} = \mathbf{F(m)}, \tag{1}$$

relates this model $\mathbf{m}$ to a dataset $\mathbf{d}$ representing four-point (Van der Pauw 1958) or 'tetrapolar' (Ragheb *et al* 1992) resistance measurements that are taken according to a measurement protocol of electrical contacts around the sample edges (Holder 2005). A popular example is the empirical 'Adjacent–Adjacent' or 'Sheffield' protocol, which uses pairs of neighboring current injection contacts in combination with pairs of neighboring voltage measurement contacts (Brown and Seagar 1987, Kauppinen *et al* 2006). Only half of these are independent (Buttiker 1988), and form what will henceforth be referred to as the *adjacent* measurement protocol.

Typically, the forward problem can be directly solved using Maxwell's equations in the form of Laplace's equation with various boundary conditions to determine the dataset from the model, as described, for example, by Holder (2005). We will define an inverse problem *method* as the selection of the model space, the data space, and the inverse algorithm by which the data space is mapped back to the model space.

The mixed-determined EIT inverse problem can be solved to linear order with consideration of noisy, non-ideal data $\mathbf{d}^{\text{obs}}$ and the selection of a reference model $\mathbf{m}^{\text{ref}}$. The experimentally observed data $\mathbf{d}^{\text{obs}}$ from the forward problem in the presence of measurement noise $\mathbf{n}$ can be written as (Braun *et al* 2017):

$$\mathbf{d}^{\text{obs}} = \mathbf{F(m)} + \mathbf{n} = \mathbf{d} + \mathbf{n}. \tag{2}$$

For a subset of models lying within linear perturbation $\Delta\mathbf{m} = \mathbf{m} - \mathbf{m}^{\text{ref}}$ of a common reference model $\mathbf{m}^{\text{ref}}$ (Grychtol and Adler 2013), the forward problem can be approximated to linear order as a deviation $\Delta\mathbf{d} = \mathbf{d}^{\text{obs}} - \mathbf{d}^{\text{ref}}$ from the inverted reference data $\mathbf{d}^{\text{ref}} = \mathbf{F}(\mathbf{m}^{\text{ref}})$:

$$\Delta\mathbf{d} = \mathbf{J}\Delta\mathbf{m} + \mathbf{n}, \tag{3}$$

where the linearized forward operation is now represented by the Jacobian matrix $\mathbf{J}$, also referred to as the sensitivity matrix, (Polydorides and Lionheart 2002, Gómez-Laberge and Adler 2008) with elements:

$$J_{\alpha\beta} = \left. \frac{\partial F_{\alpha}}{\partial m_{\beta}} \right|_{\mathbf{m}^{\text{ref}}}, \tag{4}$$

where $\alpha \in \{1, \cdots D\}$ indexes the dataset elements from 1 to the dimension D of the data space $\mathfrak{D}$, and $\beta \in \{1, \cdots M\}$ indexes the model elements from 1 to the dimension M of the model space $\mathfrak{M}$ and the derivatives are evaluated at the reference model coordinates $\mathbf{m}^{\text{ref}}$. Each Jacobian element $J_{\alpha\beta}$ quantifies the *sensitivity* of the αth data space measurement to perturbations in the βth model space component with respect to the reference model. For simplicity, in the remainder of this text $\mathbf{d}$ and $\mathbf{m}$ will refer to the linearized difference coordinates $\Delta\mathbf{d}$ and $\Delta\mathbf{m}$ relative to $\mathbf{d}^{\text{ref}}$ and $\mathbf{m}^{\text{ref}}$, respectively, in the context of the linearized problem. This work considers a homogeneous reference $\mathbf{m}^{\text{ref}}$, throughout. In general, prior knowledge can be utilized to produce more meaningful case-specific references (Grychtol and Adler 2013). The EIT inverse problem, therefore consists of mapping from an observed dataset $\mathbf{d}^{\text{obs}}$ to some model $\mathbf{m}$. In the linearized inverse problem, this is written as $\mathbf{m} = \mathbf{J}^{-g}\mathbf{d}^{\text{obs}}$, where $\mathbf{J}^{-g}$ is the generalized inverse of the Jacobian matrix $\mathbf{J}$.

Singular value decomposition (SVD) of the Jacobian is a frequently used tool for analyzing and solving the EIT inverse problem (Holder 2005). SVD decomposes the Jacobian into two unitary matrices ($\mathbf{U}, \mathbf{V}$) whose respective columns are left and right singular vectors of $\mathbf{J}$, and a diagonal matrix ($\mathbf{S}$) of singular values that are ordered from largest to smallest. This decomposition is written as

$$\mathbf{J} = \mathbf{U}\mathbf{S}\mathbf{V}^{\mathsf{T}}, \tag{5}$$

where the number of non-zero singular values in $\mathbf{S}$ is equivalent to the rank of the Jacobian (Press *et al* 2007). When $\mathbf{J}$ is square, SVD can be used to form the following inverse of $\mathbf{J}$:

$$\mathbf{J}^{-1} = \mathbf{V}\mathbf{S}^{-1}\mathbf{U}^{\mathsf{T}}. \tag{6}$$

When $\mathbf{J}$ is not square, a portion of either the data or the model space is not accessed. And depending on the measurement protocol and model parameterization, some diagonal elements of $\mathbf{S}$ may be zero or small, requiring the formation of a generalized inverse. In this case, the reciprocals of those zero and small singular values should be replaced with zeros in the inverse of $\mathbf{S}$. This replacement is referred to as truncated SVD ((T) SVD). In (T)SVD a truncation point of $k < \mathrm{rank}(\mathbf{S})$ replaces the reciprocals of small singular values to suppress the influence of noise in the inverse problem (Hansen 1990b). The Picard condition is one proposed method of selecting the truncation point k using a known data noise level (Hansen 1990a). The result is the following inverse solution in the presence of noise:

$$\mathbf{m} = \mathbf{V}_k \mathbf{S}_k^{-1} \mathbf{U}_k^{\mathsf{T}} \mathbf{d}^{\mathrm{obs}}, \tag{7}$$

where $\mathbf{m}$ is the best possible model reconstruction from the noisy data $\mathbf{d}^{\mathrm{obs}}$, $\mathbf{V}_k \mathbf{S}_k^{-1} \mathbf{U}_k^{\mathsf{T}}$ is the generalized inverse of $\mathbf{J}$, and the subscript k indicates truncation. This (T)SVD solution represents a fast and efficient way to solve the linearized inverse problem using standard methods.

3. Components of sensitivity volume method

The strategy behind the proposed sensitivity volume method as a solution to the EIT inverse problem is presented below. This method is designed to minimize susceptibility to experimental noise and maximize computational efficiency, while also being agnostic to the geometry and dimension of the EIT problem. The description of this method is broken down according to the component elements of the EIT problem, namely model space and data space selection, contact number selection, and finally the choice of solver for the linearized inverse problem. In the course of this description, the concept of a sensitivity vector is introduced to represent the fidelity of a given measurement to a weighted sum of model basis elements; a sensitivity volume figure of merit is proposed to optimize measurement protocols for targeted features; and a distinguishability criterion is generalized to assess fidelity in resolving these features.

3.1. Model space selection: $\mathfrak{M}$

Consider the full model space $\mathfrak{M}_0$ of the EIT problem with dimension M_0. Typical EIT inverse methods parameterize this full model space as a mesh defined over the volume of interest, with one independent model coordinate per mesh piece. Our strategy will be instead to choose a much smaller model subspace $\mathfrak{M} \subset \mathfrak{M}_0$ with dimension $M \ll M_0$ spanned by orthogonal basis functions comprised of linear combinations of these mesh pieces and designed to target the features of interest. Prior knowledge of the system can be used either to identify the most important features, for example, with proper orthogonal decomposition (POD) (Lipponen 2013), or, alternatively, to provide balanced resolution throughout, for example, with a harmonic polynomial series appropriate to the geometry of interest, such as Legendre polynomials, Zernike polynomials, or Fourier decomposition.

3.2. Contact number selection: C

Whereas standard EIT methods use the number of contacts C to fix the dimension D of the data space $\mathfrak{D}$, here an increased contact number C_0 will be used to define a larger data space $\mathfrak{D}_0$ of dimension D_0 greater than strictly necessary. Inside this expanded data space, an optimal *subspace* $\mathfrak{D} \subset \mathfrak{D}_0$ of dimension $D < D_0$ can be found, according to the steps in the following section. Note that under this method, contacts do not have to be equally spaced around the periphery, but can be placed arbitrarily, for example with higher density near features of interest, though for most common applications the need for uniform resolution dictates equal spacing of contacts.

Consider the dimensionality D of a desired data space and the corresponding minimum number of contacts C that spans that data space (Brown and Seagar 1987),

$$D = \frac{C(C-3)}{2}, \tag{8}$$

which can be inverted to yield the equivalent relation,

$$C = \left\lceil \frac{3}{2} + \sqrt{\frac{9}{4} + 2D} \right\rceil. \tag{9}$$

Here the ceiling function $\lceil \cdot \rceil$ ensures an integer number of contacts.

Since advantages of the sensitivity volume method come from increasing the dimensionality of the data space and therefore increasing the contact number, it is important to quantify what increase in contact number corresponds to what increase in data space dimension. If the data space is expanded to dimension D_0 by a data space inflation factor r_D,

Figure 1. Sensitivity-vectors and sensitivity volumes. (a) Data measurements d_α of circular sample on left overlaid with mesh show current injection (arrows) and voltage measurement ($+/-$) electrodes associated with $D_{\max}$ different measurement configurations. (b) In a 2D model space, the top choice of sensitivity vectors $\{\boldsymbol{\mu}_1, \boldsymbol{\mu}_2\}$ subtends a larger 2D sensitivity volume $S^{(2)}$ than the bottom $\{\boldsymbol{\mu}_1, \boldsymbol{\mu}_3\}$. (c) In the 3D case, the top sensitivity vectors $\{\boldsymbol{\mu}_1, \boldsymbol{\mu}_2, \boldsymbol{\mu}_4\}$ subtend a larger 3D volume $S^{(3)}$ than the bottom $\{\boldsymbol{\mu}_1, \boldsymbol{\mu}_3, \boldsymbol{\mu}_4\}$.

$$r_D = D_0/D, \tag{10}$$

the number of contacts must increase to C_0.

$$C_0(r_D) = \left\lceil \frac{3}{2} + \sqrt{\frac{9}{4} + 2\,r_D D} \right\rceil. \tag{11}$$

This increase can be represented with a contact number inflation factor $r_C \simeq C_0/C$, which can be determined from the above equations:

$$r_C = \frac{3}{2C} + \sqrt{r_D - \frac{3r_D}{C} + \frac{9}{4C^2}}. \tag{12}$$

Note that with a large number of contacts, the relation between r_D and r_C simplifies to $r_D \sim r_C^2$ meaning that the data space inflates roughly quadratically with the contact number.

The larger the data space inflation factor r_D, the likelier the inflated data space of dimension $D_0 = r_D D$ can contain a subspace of desired dimension D that includes only the most independent and noise-robust measurements. Note that the total number of possible four-point measurements $D_{\max}$ that can be made with arbitrarily chosen contacts is of order $\mathcal{O}(C_0{}^4)$:

$$D_{\max}(C_0) = \frac{C_0!}{(C_0 - 4)!}, \tag{13}$$

thus the search space for optimization increases geometrically with the contact number. We will refer to the list of all $D_{\max}$ possible four-point data measurements as the *measurement library*, from which D measurements will be chosen to form the candidate protocols.

3.3. Sensitivity vectors: $\boldsymbol{\mu}$

Having identified the model space $\mathfrak{M}$, the contact number and placement, and the full data space $\mathfrak{D}_0$ with total number of possible measurements $D_{\max}$, the Jacobian can now be calculated from the forward problem. Let each row of the Jacobian matrix **J** represent a sensitivity vector $\boldsymbol{\mu}_a$ in model space, composed of the sensitivity coefficients defined in equation (4),

$$\boldsymbol{\mu}_a = [J_{a1}, J_{a2}, \ldots, J_{aM}]. \tag{14}$$

As illustrated in figure 1, each sensitivity vector represents the overall sensitivity of the ath data measurement $a = \{1 \ldots D_{\max}\}$ to the set of $\beta = \{1 \ldots M\}$ orthonormal basis functions of the chosen model space. The overall sensitivity of a given measurement is thus proportional to the magnitude of its sensitivity vector.

3.4. Sensitivity volume: $S^{(D)}$

The sensitivity volume is the key figure-of-merit introduced here in order to compare and optimize choice of candidate measurement protocols. The sensitivity of a *set* of D independent measurements selected from the library of $D_{\max}$ available measurements can be quantified as the D-dimensional volume $S^{(D)}$ of a parallelotope

subtended by the chosen $\alpha = 1 \dots D$ sensitivity vector rows of the Jacobian matrix:

$$S^{(D)} = \sqrt{\det(\mathbf{J}\mathbf{J}^{\mathsf{T}})}, \tag{15}$$

as illustrated in figure 1. Conceptually, the sensitivity volume can be thought of as the product

$$S^D = \prod_{\alpha=1}^{D} |\boldsymbol{\mu}_{\alpha\perp}|, \tag{16}$$

where $\boldsymbol{\mu}_{\alpha\perp}$ is the perpendicular component of sensitivity vector α with respect to all other vectors in the set. This result is also identical to the product of the $\alpha = \{1 \dots D\}$ singular values s_α of the SVD decomposition:

$$S^{(D)} = \prod_{\alpha=1}^{D} s_\alpha. \tag{17}$$

The geometric mean S of the singular values s_α is then the average sensitivity per measurement in the data space, or the Dth root of the D-dimensional sensitivity volume, henceforth referred to as the *specific sensitivity* or in appropriate context simply the *sensitivity* of that measurement protocol:

$$S = \sqrt[D]{S^{(D)}}. \tag{18}$$

3.5. Data space selection: $\mathfrak{D}$

The data space $\mathfrak{D}$ will be chosen to have dimension D that matches that of the model space $D = M$, setting up an exactly determined inverse problem. The underdetermined case $D < M$ would leave some of the desired model space features undefined, and the overdetermined case $D > M$ would measure redundant information at the cost of computational efficiency and measurement duration. With the sensitivity volume figure-of-merit defined above, the strategy will then be to search for a data *subspace* $\mathfrak{D} \subset \mathfrak{D}_0$ with dimension $D = M$ whose measurement protocol is selected from the measurement library to have maximal sensitivity volume $S^{(D)}$ according to the chosen basis functions of our model space $\mathfrak{M}$.

3.6. Inverse solve selection: $\mathbf{J}^{-1}$

In the exact determined linearized inverse problem considered here $D = M$, the Jacobian $\mathbf{J}$ is square and invertible such that $\mathbf{J}^{-g} = \mathbf{J}^{-1}$. This makes the inverse solve in the absence of data noise computationally efficient by eliminating the need for regularization, such as Tikhonov regularization, gradient damping, or total variation regularization (Holder 2005, Menke 2012). Because of the increase in sensitivity S under the sensitivity volume method, it is less likely that truncation of singular values will be required under SVD analysis, making direct matrix inversion adequate in many cases. But in the presence of noise that exceeds the Picard condition, a simple regularization procedure, such as truncated (T)SVD, can still remove the influence of small singular values overcome by noise (Hansen 1990a). And with the dimensionality of $\mathbf{J}$ greatly reduced, there remain significant improvements in computational efficiency over T(SVD) of a standard Jacobian.

3.7. Distinguishability: z, and noise threshold: η_t

To differentiate between two model cases under increasing data noise, we generalize the distinguishability criterion z proposed by Adler *et al* (2011), Yasin *et al* (2011) and also define a noise threshold for distinguishability η_t. Consider the noiseless inverse models $\{\mathbf{m}_a, \mathbf{m}_b\}$ corresponding to two different model cases to be distinguished under noise. In the linear regime, noisy inverse solves will fall in a neighborhood around these models, described by the posterior model covariance matrix $\mathbf{C_m}$:

$$\mathbf{C_m} = \mathbf{J}^{-g}\mathbf{C_d}\mathbf{J}^{-g\mathsf{T}}, \tag{19}$$

where the data covariance matrix $\mathbf{C_d} = \eta^2\mathbf{I}$ represents, in this case, uncorrelated Gaussian experimental noise with standard deviation η, and $\mathbf{I}$ is the identity matrix. Whereas Adler *et al* identified a spatial cross-section of interest for statistical analysis, here the analysis will be conducted along a segment in model space that connects two model cases to be distinguished. A unit vector $\hat{\mathbf{u}}$ can be defined along this segment connecting the two noise-free models:

$$\hat{\mathbf{u}} = \frac{\mathbf{m}_b - \mathbf{m}_a}{|\mathbf{m}_b - \mathbf{m}_a|}, \tag{20}$$

and the component of each model's covariance $\mathbf{C_m}$ projected along this direction is:

$$\sigma_a^2 = \sigma_b^2 = \hat{u}^T C_m \hat{u}. \tag{21}$$

Following Adler *et al*, the standard deviation of the model difference σ_m becomes

$$\sigma_{\mathrm{m}}^2 = \sigma_{\mathrm{a}}^2 + \sigma_{\mathrm{b}}^2. \tag{22}$$

The result is a generalization of Adler *et al*'s distingushability z in model space:

$$z = \frac{|\mathbf{m}_{\mathrm{b}} - \mathbf{m}_{\mathrm{a}}|}{\sigma_{\mathrm{m}}}, \tag{23}$$

where $z = 1$ represents the threshold for distinguishability, and statistical significance is defined as $z > 2$ per mathematical convention (Cowan 1998).

A noise threshold η_t for distinguishability in the case of uncorrelated Gaussian noise can be determined by solving equations (19)–(23) according to the condition $z = 1$:

$$\eta_t^2 = \frac{|\mathbf{m}_{\mathrm{b}} - \mathbf{m}_{\mathrm{a}}|^2}{2\hat{\mathbf{u}}^T(\mathbf{J}^{-g}\mathbf{J}^{-g\,T})\hat{\mathbf{u}}}. \tag{24}$$

Noise exceeding this threshold renders cases $\{\mathbf{m}_{\mathrm{a}}\}$ and $\{\mathbf{m}_{\mathrm{b}}\}$ indistinguishable, *i.e.* within a standard deviation of noise of each other, and noise below half η_t means the two cases can be discerned with statistical significance.

4. The sensitivity volume method: demonstration

In the following, the sensitivity volume method will be demonstrated in two simulated scenarios, a biomedical one and an engineering one, with varying degrees of data noise to simulate experimental conditions. To illustrate the advantage of the sensitivity volume method in both cases, the inverse problem will be solved using two measurement protocols with the same number of measurements: one being the standard adjacent measurement protocol and the other being the sensitivity volume maximized measurement protocol.

The first demonstration is a simplified biomedical scenario representing interior chest imaging, which may aid in cardiac measurements of stroke volume and ejection fraction that can diagnose dangerous cardiac conditions such as heart failure and coronary syndrome (Zlochiver *et al* 2006, Proenca *et al* 2014, Rao *et al* 2018, Putensen *et al* 2019). The second demonstration is a structural engineering example since maintenance inspections of historical structures or enforcement of building codes may require identifying the number of reinforcement rods present in a concrete pillar. Various individual steps of the simulation employed the EIDORS EIT package (Adler and Lionheart 2006), including mesh building and plotting. The results of the biomedical and engineering demonstrations are shown in figures 3 and 4, respectively.

4.1. Model space selection: demonstration

According to the sensitivity volume method, one first chooses a reduced model space ($M < M_0$) that will have sufficient feature resolution. Given the circular symmetry of this test problem, the results of POD from Allers and Santosa (Allers and Santosa 1991) and from Lipponen *et al* (2013) suggest that Zernike polynomials shown in figure 2 defined over a mesh will provide an excellent empirical basis for model space parameterization. The orthonormal Zernike polynomial functions are defined on a unit disk in terms of polar coordinates $Z_n^h(r, \theta)$, with increasing radial order $n = \{0, \dots N\}$ and angular order $h = \{-n, -n + 2, \dots n - 2, n\}$ representing increasing resolution where N is the highest polynomial order of the Zernike polynomials used (Lakshminarayanan and Fleck 2011):

$$Z_n^h(r, \theta) = \begin{cases} F_n^h R_n^{|h|} r \cos(h\theta) & \text{for } h \geqslant 0, \\ -F_n^h R_n^{|h|} r \sin(h\theta) & \text{for } h < 0, \end{cases} \tag{25}$$
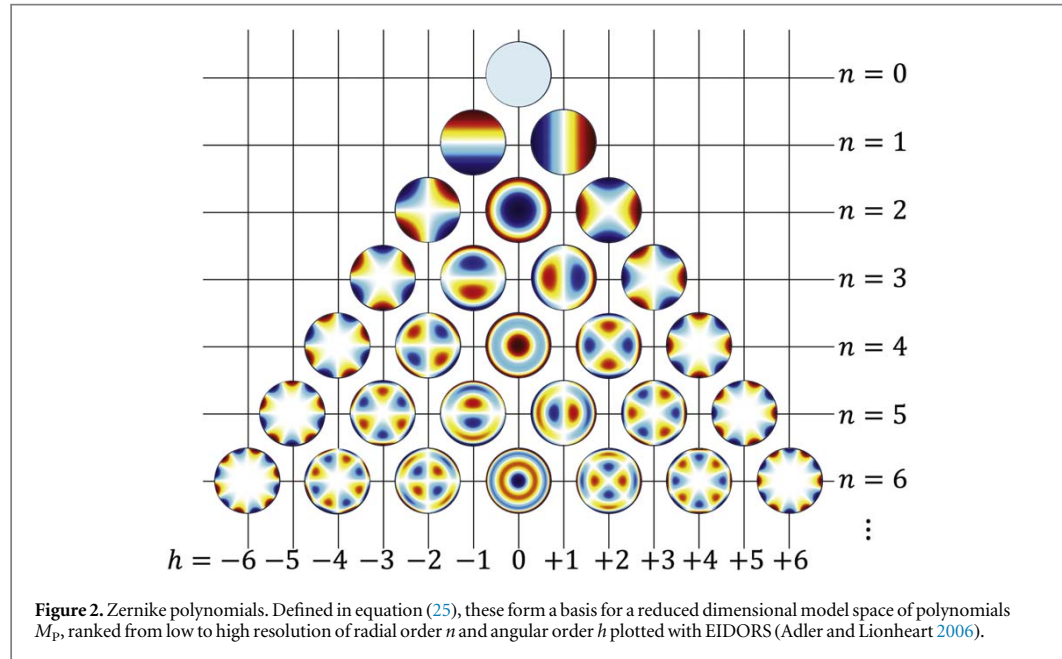
where $R_n^{|h|}$ is defined as

$$R_n^{|h|}(r) = \sum_{l=0}^{\frac{n-h}{2}} \frac{(-1)^l (n-l)!}{l!\left(\frac{n+h}{2} - l\right)!\left(\frac{n-h}{2} - l\right)!} r^{n-2l}. \tag{26}$$

The normalization prefactor F_n^h is

$$F_n^h = \sqrt{\frac{2(n+1)}{1 + \delta_{h0}}}, \tag{27}$$

where δ_{h0} is the Kronecker delta function (Lakshminarayanan and Fleck 2011). Using this polynomial basis, any conductivity map can be represented as a linear combination of Zernike polynomials:

Figure 2. Zernike polynomials. Defined in equation (25), these form a basis for a reduced dimensional model space of polynomials M_P, ranked from low to high resolution of radial order n and angular order h plotted with EIDORS (Adler and Lionheart 2006).

$$\sigma(r, \theta) = \sigma_0(r, \theta) + \sum_{n=0}^{N} \sum_{h=-n,-n+2,\ldots}^{n} m_{n,h} Z_n^h(r, \theta),$$ (28)

where $\sigma_0(r, \theta)$ is the reference, chosen here to be homogeneous.

For a given polynomial order N, the dimension M_P of the polynomial model space up to and including that order is:

$$M_P = \frac{(N+1)(N+2)}{2}.$$ (29)

In practice, the order N of the polynomial will be chosen large enough that $M_P \geqslant M$, and the specific M polynomials for the model space basis are chosen to suit prior knowledge of electrode symmetries and the desired resolution of the problem at hand. Thus, the model conductivity **m** is represented here as a vector of length M describing the set of weights for each polynomial $m_{n,h}$.

To deploy these continuous basis functions in a finite element solver, Zernike polynomials (Fricker 2023) were projected onto a fine mesh generated in EIDORS with Netgen (Adler and Lionheart 2006). An $M_0 \times M$-dimensional mapping matrix **Z** transforms the M-dimensional model vector **m** in the polynomial basis into a M_0-dimensional vector $\mathbf{m}^{\text{mesh}}$ on a finite element mesh,

$$\mathbf{m}^{\text{mesh}} = \mathbf{Z}\,\mathbf{m}.$$ (30)

The same mapping matrix **Z** maps a $D \times M_0$-dimensional Jacobian $\mathbf{J}^{\text{mesh}}$ derived on a finite element mesh into a $D \times M$-dimensional Jacobian **J**:

$$\mathbf{J}^{\text{mesh}}\,\mathbf{Z} = \mathbf{J},$$ (31)

where each of M columns of **Z** corresponds to the mesh-element parameterization of each continuous Zernike polynomial. As a result, the forward problem can be written as:

$$\mathbf{d} = \mathbf{J}\mathbf{m} = \mathbf{J}^{\text{mesh}}\mathbf{m}^{\text{mesh}}.$$ (32)

For the biomedical example of a 'normal' versus 'enlarged heart,' $M = 27$ independent standard Zernike polynomials of increasing resolution were chosen up through order $N = 6$. This uniform resolution model space is represented by all the polynomials plotted in figure 2 except for the bottom center $n = 6$; $h = 0$. For the engineering example comparing 3 versus 6 reinforcement rods, prior knowledge that the system of interest had either 3-fold or 6-fold rotational symmetry allowed the $M = 27$-dimensional model space to be constrained, accordingly. Here, this model space is represented by the first $M = 27$ standard Zernike polynomial functions that satisfy the 3- and 6-fold symmetry requirements, requiring the sampling of polynomials up to order $N = 12$. In both cases, a homogeneous constant background was used as a reference, and the higher conductivity test features were given a 20% enhancement in the conductivity.

4.2. Contact number selection: demonstration

For both examples, the contacts are equally spaced at the circumference with the number of contacts set according to equation (11). In order to have $D = M = 27$ measurements, we find for the adjacent measurement protocol that an uninflated $r_D = 1$ data space (and uninflated contact number $r_C = 1$) requires $C_0 = C = 9$ contacts. For the sensitivity volume measurement protocol, an inflated data space with $r_D = 12$ gives overall dimension $D_0 = r_D D = 324$ which requires $C_0 = 3C = 27$ contacts per equation (11). It is observed that when using Zernike polynomials as the model space basis, an odd number of contacts C_0 is preferred to minimize the null space at the maximum radial order $n = N$.

4.3. Sensitivity vectors: demonstration

For the inflated data space with $C_0 = 27$ contacts, sensitivity vectors for both the biomedical and engineering examples were calculated per equation (14) for all $D_{max}(C_0) = 421,\,200$ possible measurements. These calculations used the default EIDORS forward solver with the adjoint Jacobian (Vauhkonen *et al* 2001, Adler and Lionheart 2006) on a homogeneous reference, along with appropriate mapping matrices **Z** per equation (30) for each scenario's model space. The resulting libraries of D_{max} sensitivity vectors formed measurement search spaces for the two respective cases.

4.4. Sensitivity volume: demonstration

Sensitivity volumes were determined for each case per equation (17) for various measurement protocols with $D = M = 27$ sensitivity vectors chosen from the library of D_{max} available. The sensitivity volumes are then compared to find which D out of D_{max} specific vectors maximizes the sensitivity volume figure-of-merit $S^{(D)}$. Various search algorithms can be implemented such as a greedy search (Williamson and Shmoys 2011), genetic search (Press *et al* 2007), or simulated annealing (Press *et al* 2007) to find this measurement protocol with maximum sensitivity volume. In the examples below, a modified greedy search was implemented.

4.5. Data space selection: demonstration

Table 1 shows the sensitivity volume optimized protocol for data space measurements for the biological and engineering scenarios, respectively. Just over half of these measurements (highlighted) have a similar configuration whereby the current injection electrode I^+ neighbors the positive voltage V^+ electrode, the current sink I^- neighbors the negative voltage V^-, and the inner/outer pairs are of the same type, either current or voltage. Because the contacts of this frequent configuration are the same as an adjacent configuration but functionally rotated analogous to a Van der Pauw conjugate measurement (Van der Pauw 1958), this contact configuration will be referred to as the 'adjacent–conjugate' configuration. But it should be pointed out that the resulting measurements in the protocols do not follow a rotational symmetry like the adjacent or skip measurement protocols and could not have been empirically guessed in advance. Furthermore, the biological problem with its uniform resolution model results in a rather different measurement protocol than the engineering problem with its 3/6-fold constrained symmetry, illustrating the dependence of the measurement protocol on the model structure.

We reiterate that once an optimal measurement protocol is determined, there is no need to repeat the sensitivity volume optimization. Because the computationally intensive steps of sections 4.3 through 4.5 are performed in advance to generate the Jacobian for the optimized data space, the inverse solve can now be extremely rapid, as fast as a simple matrix multiplication.

4.6. Inverse solver selection: demonstration

To complete the sensitivity volume method, one must solve the resultant exact determined inverse problem ($M = D$). A Matlab code was written to use (truncated) singular value decomposition (T)SVD to solve the linearized, non-iterative inverse problem for orthogonal polynomial model spaces per equation (7). Data was simulated using EIDORS' default forward solver and a finite element mesh. Gaussian noise with standard deviation η was added to the simulated data to emulate realistic experimental conditions.

4.7. Distinguishability and noise threshold: demonstration

In the biomedical example, our SVD solver was used with no truncation of singular values. Figure 3(a) shows the 'input' conductivity maps in the forward problem for the 'normal' heart (top) and the 'enlarged' heart (bottom) using an EIDORS derived mesh. Reconstructed conductivity maps of the noiseless ($\eta = 0$) normal and enlarged heart are shown in color in the left of panel (b) for the standard adjacent measurement protocol, and the left of panel (c) for the sensitivity volume maximized measurement protocol. The polynomial model space in section 4.1 and the inverse solver described in section 4.6 were used to produce reconstructed images from simulated datasets using both measurement protocols. In the absence of noise, all reconstructions show similar
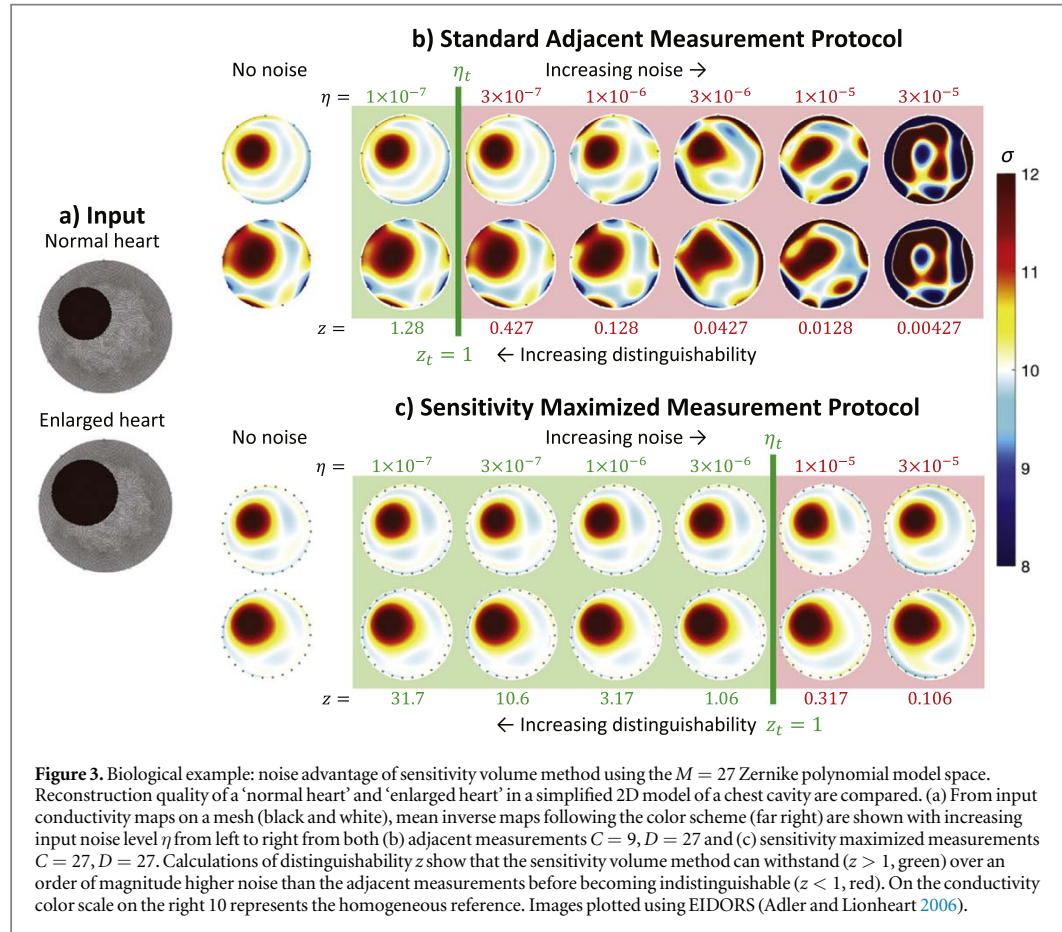
Table 1. Measurement protocols for the biomedical and engineering examples, with current injection between I^+ and I^- electrodes and voltage measurement across electrodes V^+ and V^-. More than half the measurements (highlighted in grey) are of a similar configuration which we define to as 'adjacent–conjugate,' whereby each voltage electrode neighbors a current electrode, and the inner/outer pairs are current/voltage electrodes.

Index	Biomedical case					Engineering case			
	I^+	I^-	V^+	V^-		I^+	I^-	V^+	V^-
1	1	4	2	3		1	17	18	27
2	1	14	2	15		1	18	7	24
3	1	26	2	25		1	20	2	19
4	2	5	6	27		2	7	4	6
5	3	12	4	11		2	25	3	23
6	3	23	5	22		3	11	10	18
7	4	8	5	7		3	21	4	20
8	4	11	6	9		4	11	5	9
9	5	15	6	14		4	13	6	15
10	6	21	8	19		5	8	6	7
11	7	11	8	10		5	15	6	14
12	7	14	9	12		5	22	16	26
13	7	27	8	25		7	10	8	9
14	9	18	10	17		7	17	8	16
15	9	24	11	22		8	11	9	12
16	10	14	11	13		9	18	12	21
17	10	16	12	15		10	21	12	19
18	12	21	13	20		10	24	11	23
19	13	20	15	18		11	14	12	13
20	14	17	15	16		11	20	14	23
21	15	25	16	24		12	23	13	22
22	16	20	17	19		13	26	14	25
23	16	23	18	21		14	16	15	18
24	18	27	19	26		15	19	16	18
25	19	23	20	22		17	20	18	19
26	19	26	21	24		22	26	23	25
27	22	26	23	25		24	27	25	26

resolution, with the exception that the enlarged case for the adjacent measurement protocol shows artifacts with residual oscillations at the periphery.

To investigate noise tolerance, the mean results of 1000 simulated SVD inversions of normal and enlarged hearts were generated with increased data noise η. As noise increases to the right in figure 3, the standard adjacent measurements in the top rows generate average inverse maps that deviate further from the noiseless reconstructions, and eventually become overwhelmed by the noise. By contrast, reconstructions using sensitivity volume derived measurements in the bottom rows can withstand over an order of magnitude more noise than the adjacent measurements.

The results can be quantified using the distinguishability and noise tolerance metrics of Subsection 3.7. The distinguishability z was calculated at each noise level η for reconstruction of both adjacent and sensitivity maximized measurement protocols. The distinguishability threshold is defined as $z = 1$, whereupon the normal and enlarged cases become statistically indistinguishable, and η_t is the corresponding noise level threshold. For $z > 1$, the average inverse maps begin to show differences from the noise-free scenario, and $z = 2$ represents the threshold for statistically significant distinguishability (Cowan 1998). The noise threshold η_t for both cases is

Figure 3. Biological example: noise advantage of sensitivity volume method using the $M = 27$ Zernike polynomial model space. Reconstruction quality of a 'normal heart' and 'enlarged heart' in a simplified 2D model of a chest cavity are compared. (a) From input conductivity maps on a mesh (black and white), mean inverse maps following the color scheme (far right) are shown with increasing input noise level η from left to right from both (b) adjacent measurements $C = 9, D = 27$ and (c) sensitivity maximized measurements $C = 27, D = 27$. Calculations of distinguishability z show that the sensitivity volume method can withstand ($z > 1$, green) over an order of magnitude higher noise than the adjacent measurements before becoming indistinguishable ($z < 1$, red). On the conductivity color scale on the right 10 represents the homogeneous reference. Images plotted using EIDORS (Adler and Lionheart 2006).
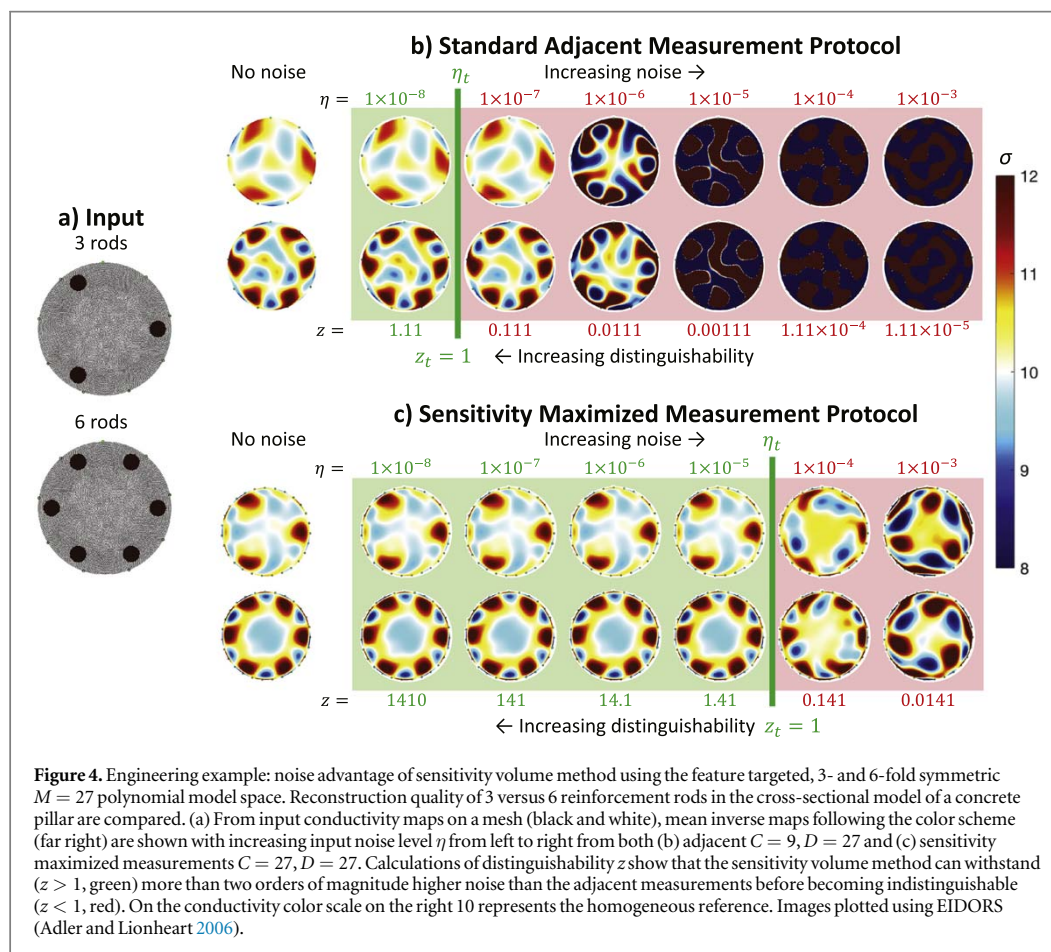
Table 2. Noise tolerance of sensitivity volume measurement protocol compared to adjacent measurement protocol. Although the protocols differ in contact number C, they have the same number of data space measurements D and model space dimensions M. Nonetheless, the sensitivity volume protocol shows significantly larger noise thresholds η_t and significantly larger sensitivity S/S_0 normalized relative to the adjacent case, exceeding an order of magnitude for the biomedical case (figure 3) and two orders of magnitude for the engineering case (figure 4).

Measurement protocol				Biomedical case		Engineering case	
	C	D	M	η_t	S/S_0	η_t	S/S_0
Adjacent	9	27	27	0.13×10^{-6}	1	0.011×10^{-6}	1
Sensitivity	27	27	27	$3.2 \ \times 10^{-6}$	10.8	$14 \ \times 10^{-6}$	236

listed in table 2 and shows that the sensitivity volume maximized dataset tolerates a factor of 25 × more noise than the adjacent measurement protocol, with the *same number* of measurements. Table 2 also lists the increase in relative sensitivity S/S_0 of the sensitivity volume measurement protocol from equation (18) relative to that of the adjacent measurement protocol.

In the engineering example, our (T)SVD solver was used for both measurement protocols with a truncation point of $k = 18$ singular values, as necessitated by smaller amplitudes of the singular values from the Jacobian matrices. Figure 4(a) shows the forward problem input maps of 3 rods (top) and 6 rods (bottom). Reconstructed conductivity maps of the noiseless ($\eta = 0$) cases are shown in color in the left of panel (b) for the standard adjacent measurement protocol, and the left of panel (c) for the sensitivity volume maximized measurement protocol. Datasets generated using both measurement protocols were reconstructed using the 3- and 6-fold symmetric polynomial model space described in section 4.1. Once again, the mean results of 1000 (T)SVD inverse solves are generated with increasing noise η from left to right. In the reconstructions from adjacent measurements in panel (b), small singular values in the (T)SVD inversion cause the noise to rapidly overtake any meaningful model features. In contrast, sensitivity volume maximized measurements in panel (c), can withstand
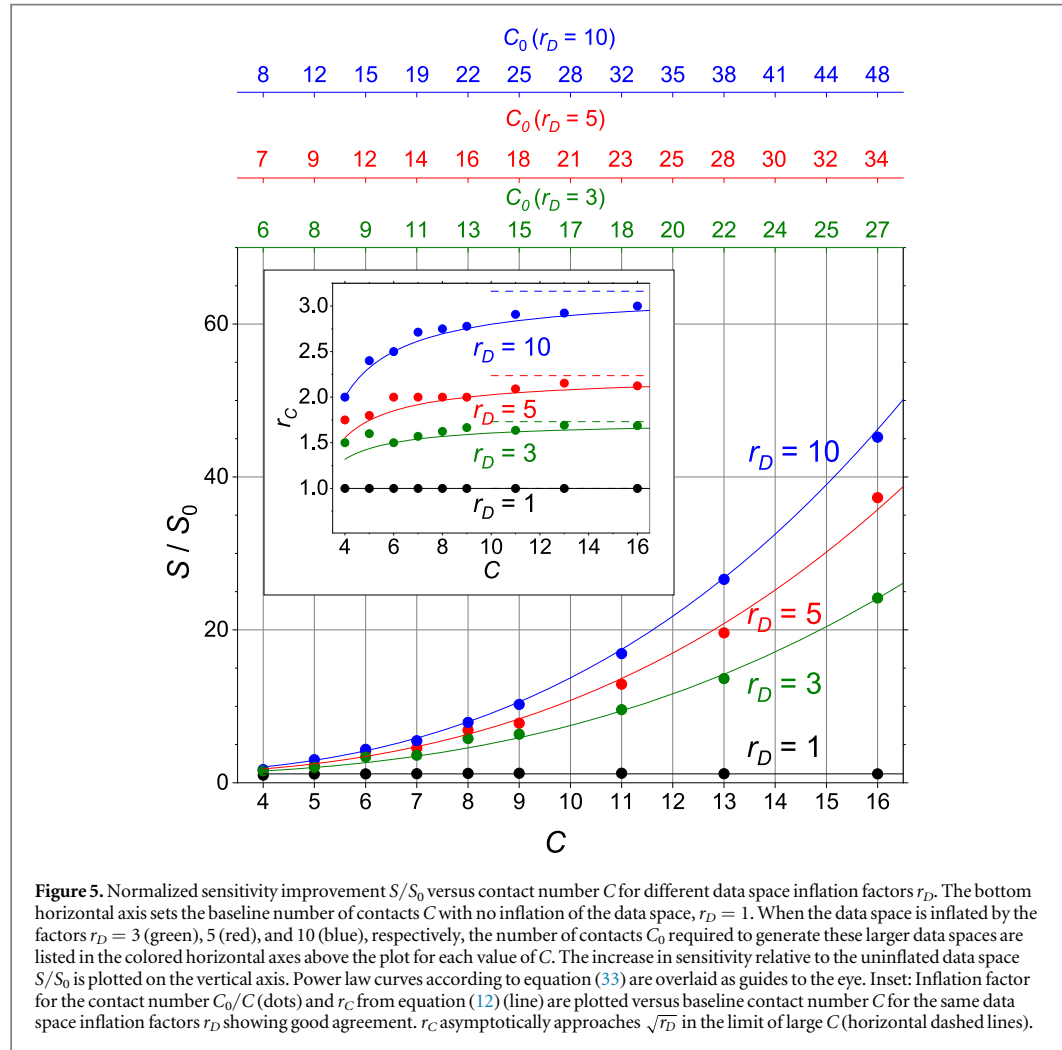
Figure 4. Engineering example: noise advantage of sensitivity volume method using the feature targeted, 3- and 6-fold symmetric $M = 27$ polynomial model space. Reconstruction quality of 3 versus 6 reinforcement rods in the cross-sectional model of a concrete pillar are compared. (a) From input conductivity maps on a mesh (black and white), mean inverse maps following the color scheme (far right) are shown with increasing input noise level η from left to right from both (b) adjacent $C = 9, D = 27$ and (c) sensitivity maximized measurements $C = 27, D = 27$. Calculations of distinguishability z show that the sensitivity volume method can withstand ($z > 1$, green) more than two orders of magnitude higher noise than the adjacent measurements before becoming indistinguishable ($z < 1$, red). On the conductivity color scale on the right 10 represents the homogeneous reference. Images plotted using EIDORS (Adler and Lionheart 2006).

three orders of magnitude more noise before such model obfuscation occurs, with the respective η_t values again listed in table 2.

4.8. Iterative versus non-iterative solvers: optimizing computational speed

The final advantage of the sensitivity volume method is to leverage the gain in sensitivity to achieve faster computational time. A rapid refresh rate for tomographic mapping is important in applications where the system under study is dynamically varying, such as a beating heart or a structural element under imminent failure. But when solving inverse problems in the presence of data noise, it is typically necessary to rely on an iterative solver which can slow down the inversion algorithm.

Here, a standard iterative solver is challenged against the non-iterative sensitivity volume method with the same distinguishability problem for the biomedical and engineering cases, above. The noise threshold, and its computation times were compared to the computation times of our non-iterative sensitivity volume method under the same noise level. The iterative solver to be compared is the publicly available EIDORS iterative Gauss Newton inverse solver (Adler and Lionheart 2006), which can conduct inverse solves in 100 or fewer iterations with the regularizing hyperparameter set to 1×10^{-7}. For calculations of the EIDORS noise threshold, the model covariance was estimated from ensembles of 100 different inverse solves for different noise amplitudes η, and the resulting noise thresholds are listed in table 3. The noise threshold of the iterative EIDORS regularized inversion with the adjacent data space, is always of the same order of magnitude and slightly less than the noise tolerated by the non-iterative (T)SVD inversion with the sensitivity volume method. Table 3 shows the significant speed advantage of inverting with the non-iterative sensitivity volume method over inverting with a regularized, iterative solver by comparing their computation times t_c for the examples shown previously. The sensitivity volume method produces results in approximately $1/600\,000^{\text{th}}$ the computation time of the EIDORS inverse solver.

Figure 5. Normalized sensitivity improvement S/S_0 versus contact number C for different data space inflation factors r_D. The bottom horizontal axis sets the baseline number of contacts C with no inflation of the data space, $r_D = 1$. When the data space is inflated by the factors $r_D = 3$ (green), 5 (red), and 10 (blue), respectively, the number of contacts C_0 required to generate these larger data spaces are listed in the colored horizontal axes above the plot for each value of C. The increase in sensitivity relative to the uninflated data space S/S_0 is plotted on the vertical axis. Power law curves according to equation (33) are overlaid as guides to the eye. Inset: Inflation factor for the contact number C_0/C (dots) and r_C from equation (12) (line) are plotted versus baseline contact number C for the same data space inflation factors r_D showing good agreement. r_C asymptotically approaches $\sqrt{r_D}$ in the limit of large C (horizontal dashed lines).

Table 3. Computational advantage of sensitivity volume method over default EIDORS inverse solvers. Comparisons of computation times t_c and noise thresholds η_t show the sensitivity volume method can produce comparable noise-tolerance to EIDORS but 600 000× faster.

Inverse Solver	Biomedical case		Engineering case	
	t_c	η_t	t_c	η_t
EIDORS	69 s	1.7×10^{-6}	67 s	3.1×10^{-6}
Sensitivity	110 μs	3.2×10^{-6}	110 μs	14×10^{-6}

4.9. Inflated versus uninflated data spaces

In the sensitivity volume method, inflating the data space comes at a cost of adding more contacts. Thus, it is important to quantify the degree to which an inflation of the data space leads to an improvement in the overall sensitivity. A computational study of the sensitivity for a 2D circle was undertaken for various data space inflation factors $r_D = 1, 3, 5$, and 10 with equally spaced circumferential contacts, a homogeneous reference, and a Zernike polynomial model space, and the corresponding factor of increase in contact number r_C was compared.

In figure 5, the initial number of contacts C listed on the bottom axis will set the baseline data space dimension D per equation (8). Then this data space will be increased by the factor r_D to the value D_0, requiring that the contact number also be correspondingly increased to $C_0(r_D)$ listed along the top axis of figure 5 per equation (9). The inset of figure 5 compares the exact value by which the contact number is inflated $C_0(r_D)/C$ (filled circles) along with the analytical expression for r_C from equation (12) (solid lines), showing good

agreement. In particular, equation (12) predicts that the r_C factor saturates at $r_C = \sqrt{r_D}$ for large contact number (dashed horizontal lines), with this saturation evident already for $C > 10$.

The sensitivity improvement S is then plotted on the vertical axis of figure 5 relative to the adjacent measurement protocol S_0. The behavior reveals significant increase in the sensitivity ratio S/S_0 by one-and-a-half orders of magnitude as the data space D_0 expands by increasing factors of r_D, and this enhanced sensitivity is most dramatic with the largest number of contacts. For convenience, the following empirical expression for the sensitivity enhancement can serve as a guide to the eye, plotted as continuous curves in figure 5

$$\frac{S}{S_0} \simeq 1 + \left(\frac{C}{C'(r_D)}\right)^{2.7}, \tag{33}$$

with the empirical parameter $C'(r_D)$ of the plots of figure 5 found to be $C'(3) = 5.0$, $C'(5) = 4.3$, and $C'(10) = 3.9$. Equation (33) can be inverted to determine roughly how many contacts would be needed to achieve a desired increase in sensitivity S/S_0 over the adjacent protocol

$$C \simeq C'(r_D)\left(\frac{S}{S_0} - 1\right)^{1/2.7}. \tag{34}$$

Note that large gains in sensitivity can be achieved with only a modest inflation factor. As shown in the inset for the case of $r_D = 3$ and assuming an initial $C = 11$ contacts, the number of contacts only needs to be increased by 65% to $C_0 = 18$ contacts to result in more than an order of magnitude improvement in sensitivity S/S_0. As another example, for an initial $C = 16$ contacts common in EIT systems, an increase in contact number to $C_0 = 27$ will increase the signal-to-noise by a factor of $\times 25$. The sensitivity can be further increased with an increase in the data space scaling factor to $r_D = 5$ or $r_D = 10$ corresponding to approximately twice ($r_C = 2$) or triple ($r_C = 3$) the number of contacts.

As an aside, we note that without increasing the number of contacts ($r_D = r_C = 1$), the sensitivity volume method does not show significant improvement over the adjacent or skip (Adler *et al* 2011) data sets in this general case of a homogeneous disc, achieving at most a 20% improvement in S/S_0. Such gains show why the adjacent data space has stood the test of time as a popular empirical rule for choosing a 2D data space. But in the case of an inhomogeneous reference, a restricted model space such as the engineering example of figure 4, or irregular geometries, the sensitivity volume method is expected to show performance advantages.

5. Alternate optimization strategies

Alternative EIT method optimization efforts are categorized below according to the optimization parameter of interest, and contextualized relative to the sensitivity volume method introduced above for comparison.

5.1. Model space selection: method comparison
The strategic choice of a model space in the sensitivity volume method was informed by prior work within the EIT literature, wherein this choice has also been referred to as selection of the 'model' (Lipponen *et al* 2013), choice of 'conductivity basis functions' (Tang *et al* 2002), or the 'parameterization of the domain' (Boyle *et al* 2012). Reduced dimensionality model spaces can be constructed using prior knowledge (Vauhkonen *et al* 1997, Tang *et al* 2002) to significantly decrease computation time (Gómez-Laberge and Adler 2008, Boyle *et al* 2012). For example, Lipponen *et al* (2013) used POD to produce orthonormal functions that strongly resembled Zernike polynomials, a known set of orthonormal polynomial functions used by Allers and Santosa as a model space basis for a 2D circular sample (Allers and Santosa 1991). In keeping with the spirit of the above examples, the sensitivity volume method, leverages the advantage of a reduced model space.

5.2. Contact selection: method comparison
Other EIT literature has sought to increase contact number (Coxson *et al* 2022) and vary contact placement (Yan *et al* 2006, Smyl and Liu 2020, Karimi *et al* 2021) to optimize results. Additional works have used two-point measurements or electrode segmentation schemes to select contacts (Polydorides and McCann 2002, Kantartzis *et al* 2013, Zhang *et al* 2016, Ma *et al* 2020) that may have some strict mathematical advantage, but are disadvantageous for use in biomedical applications (Putensen *et al* 2019) or with existing EIT hardware. Although these works have considered the effect of contacts on the EIT problem, the proposed sensitivity volume method offers a specific figure of merit to optimize contact number and placement.

5.3. Sensitivity and EIT: method comparison
The use of the term 'sensitivity' in relation to EIT is borrowed from the common alias of the Jacobian as the 'sensitivity matrix' (Holder 2005). The sensitivities of different prescribed measurement protocols have been

compared by examining the matrices derived from singular value decomposition (Polydorides and McCann 2002, Tang *et al* 2002, Graham and Adler 2007, Kantartzis *et al* 2013). Other sensitivity-based figures of merit are limited to model spaces comprised of the full finite element mesh $\mathfrak{M}_0$ (Grychtol *et al* 2019, Coxson *et al* 2022) or require subjective visual judgements (Kauppinen *et al* 2006, Paldanius *et al* 2022). The sensitivity volume parameter proposed here, by contrast, is a mathematically precise, objective scalar representing the overall sensitivity of a set of measurements.

5.4. Figures of merit for optimization: method comparison

In the optimization of EIT methods, it becomes necessary to develop figures of merit for quantitative comparisons. A wide variety of metrics have been proposed within the EIT literature that are often case specific (Graham and Adler 2006, 2007, Adler *et al* 2009, 2011, Yasin *et al* 2011, Grychtol *et al* 2016, Wagenaar and Adler 2016, Thürk *et al* 2019) or cannot be applied until after an inverse solve is completed (Yorkey *et al* 1987, Tang *et al* 2002, Coxson *et al* 2022). In comparison, the sensitivity volume figure-of-merit is unique, unambiguous, consistent, and broadly applicable.

5.5. Data space selection: method comparison

Data space selection has been referred to as an 'electrode selection algorithm' (Coxson *et al* 2022), a measurement 'protocol' (Holder 2005), an 'electrode stimulation and measurement configuration' (Grychtol *et al* 2016), or an 'electrode placement configuration' (Graham and Adler 2007). These prior works often take trial and error approaches (Adler *et al* 2011), are limited to highly specific cases (Ma *et al* 2020), or require optimization of multi-step machine learning algorithms (Coxson *et al* 2022). In addition to the adjacent measurement protocol mentioned in the introduction, skip measurements have grown in popularity as a data space standard based on an empirical extrapolation of adjacent data space (Adler *et al* 2011, de Castro Martins *et al* 2019, Adler and Zhao 2023). In the sensitivity volume method, by contrast, increased *data importance* is achieved by selecting current and voltage contacts not empirically, but according to a maximized figure-of-merit.

5.6. Inverse solver: method comparison

The EIT literature seeks to maximize *computational efficiency* in solving the inverse problem. To this end, small model space dimensions have been recommended to reduce the ill-posed nature of the problem and decrease computation time (Vauhkonen *et al* 1997, Tang *et al* 2002), despite the continued prevalence of large model spaces with $M \gg D$. In contrast, by solving an exact-determined problem $M = D$, the sensitivity volume method quickly solves EIT with less regularization. A comparison computational efficiency (Yorkey *et al* 1987, Gómez-Laberge and Adler 2008, Boyle *et al* 2012, Lipponen *et al* 2013) is shown in section 4 to demonstrate this advantage.

The ill-posedness and inherently nonlinear nature of the EIT problem often necessitates iterative solutions, such as those available in the popular open source Matlab package EIDORS (Vauhkonen *et al* 2001, Adler and Lionheart 2006, Graham and Adler 2006). Whereas the treatment in this manuscript has focused on the linearized problem, we note that the *a priori* calculations in the sensitivity volume method can also be implemented prior to solving the nonlinear problem and provide the same advantages in noise robustness. It should be noted that one does not need to use the reduced basis model space for inversion. One may merely use the sensitivity volume method to generate a measurement protocol with high sensitivity, and then use any favored EIT inverse solver to convert those highly sensitive data measurements to an image reconstruction.

5.7. Distinguishability and noise tolerance metrics: method comparison

In addition to the metric proposed by Adler *et al* (2011), Yasin *et al* (2011), Adler and Zhao (2023) and generalized in section 3.7, other measures of distinguishability have been proposed in the EIT literature (Vauhkonen *et al* 1997, Graham and Adler 2007, Adler *et al* 2009, Braun *et al* 2017). For example, Isaacson (1986), Gisser *et al* (1988) defined distinguishability in terms of current patterns using all electrodes. But hardware capabilities, current limits, and the inconvenience of optimization during measurement limited use of these maximal distinguishability patterns (Holder 2005). In contrast, the sensitivity volume method uses pair drive current patterns and *a priori* calculations to optimize measurements for existing EIT systems and achieve improvements in signal to noise.

6. Conclusions

This manuscript details a sensitivity volume method for optimizing the EIT inverse-problem for increased noise robustness of measurements and improved *computational efficiency*. The above analysis demonstrates the

benefit of targeted selection of model space, data space, and inverse solver for increased *data importance* by leveraging prior information and introducing the sensitivity volume figure of merit. The sensitivity volume method chooses a model space of targeted features in which to optimize and solve the EIT problem, identifies an appropriate contact number to inflate the available data space, selects the data subspace with the largest sensitivity volume, and finally, solves an exact-determined inverse problem. In the simulated examples presented to illustrate our methods, we observed a factor of over two orders of magnitude improvement in noise tolerance compared to a standard EIT model space, data space, and inverse solver choice, or $\times 600\,000$ improvement in computation time over iterative solvers with comparable fidelity. The proposed sensitivity volume method makes important steps towards the goal of rapid-refresh, noise-robust, high-resolution EIT inversion.

Acknowledgments

Data availability statement

The data in this study are most easily reproduced using the simple step by step models described in the manuscript. The code for generating the data is likewise described step by step in the manuscript. The specific code that we have implemented and the specific 18 000 element meshes are nonetheless available upon request. The data that support the findings of this study are available upon reasonable request from the authors.

ORCID iDs

Claire C Onsager ⬤ https://orcid.org/0000-0002-1993-6103
Chulin Wang ⬤ https://orcid.org/0000-0002-1877-3445
Can C Aygen ⬤ https://orcid.org/0000-0001-9129-5710
Lauren Lang ⬤ https://orcid.org/0000-0003-2222-9407
Suzan van der Lee ⬤ https://orcid.org/0000-0003-1884-1185
Matthew A Grayson ⬤ https://orcid.org/0000-0003-4914-5043

References

Adler A, Gaggero P O and Maimaitijiang Y 2011 Adjacent stimulation and measurement patterns considered harmful *Physiol. Meas.* **32** 731–44
Adler A and Lionheart W R B 2006 Uses and abuses of EIDORS: an extensible software base for EIT *Physiol. Meas.* **27** S25–42
Adler A and Zhao Z 2023 Resolution as a function of stimulation and measurement patterns *Proc. of the 23rd Int. Conf. on Biomedical Applications of Electrical Impedance Tomography (EIT2023)* ed F Röhren *et al* p 68
Adler A *et al* 2009 GREIT: a unified approach to 2D linear EIT reconstruction of lung images *Physiol. Meas.* **30** S35–55
Allers A and Santosa F 1991 Stability and resolution analysis of a linearized problem in electrical impedance tomography *Inverse Prob.* **7** 515–33
Boyle A, Borsic A and Adler A 2012 Addressing the computational cost of large EIT solutions *Physiol. Meas.* **33** 787–800
Braun F, Proença M, Solà J, Thiran J P and Adler A 2017 A versatile noise performance metric for electrical impedance tomography algorithms *IEEE Trans. Biomed. Eng.* **64** 2321–30
Brown B H and Seagar A D 1987 The sheffield data collection system *Clin. Phys. Physiol. Meas.* **8** 91–7
Buttiker M 1988 Symmetry of electrical conduction *IBM J. Res. Dev.* **32** 317–34
Cowan G 1998 *Statistical Data Analysis* (Oxford University Press)
Coxson A *et al* 2022 Machine learning enhanced electrical impedance tomography for 2D materials *Inverse Prob.* **38** 085007
de Castro Martins T *et al* 2019 A review of electrical impedance tomography in lung applications: theory and algorithms for absolute images *Ann. Rev. Control* **48** 442–71
Ducut J D, Alipio M, Go P J, Concepcion R II, Vicerra R R, Bandala A and Dadios E 2022 A review of electrical resistivity tomography applications in underground imaging and object detection *Displays* **73** 102208
Fricker P 2023 Zernike polynomials, version 1.3.0.1 *MATLAB Central File Exchange* https://mathworks.com/matlabcentral/fileexchange/7687-zernike-polynomials
Gisser D G, Isaacson D and Newell J C 1988 Theory and performance of an adaptive current tomography system *Clin. Phys. Physiol. Meas.* **9** 35–41
Gómez-Laberge C and Adler A 2008 Direct EIT jacobian calculations for conductivity change and electrode movement *Physiol. Meas.* **29** S89–99
Graham B M and Adler A 2006 Objective selection of hyperparameter for EIT *Physiol. Meas.* **27** S65–79
Graham B M and Adler A 2007 Electrode placement configurations for 3D EIT *Physiol. Meas.* **28** S29–44
Grychtol B and Adler A 2013 Uniform background assumption produces misleading lung EIT images *Physiol. Meas.* **34** 579–93
Grychtol B, Müller B and Adler A 2016 3D EIT image reconstruction with GREIT *Physiol. Meas.* **37** 785–800

Grychtol B, Schramel J P, Braun F, Riedel T, Auer U, Mosing M, Braun C, Waldmann A D, Böhm S H and Adler A 2019 Thoracic EIT in 3D: experiences and recommendations *Physiol. Meas.* **40** 074006

Hansen P C 1990a The discrete picard condition for discrete ill-posed problems *BIT Num. Math.* **30** 658–72

Hansen P C 1990b Truncated singular value decomposition solutions to discrete ill-posed problems with ill-determined numerical rank *SIAM J. Sci. Stat. Comput.* **11** 503–18

Holder D S 2005 *Electrical Impedance Tomography: Methods, History and Applications* (Institute of Physics Publishing)

Isaacson D 1986 Distinguishability of conductivities by electric current computed tomography *IEEE Trans. Med. Imaging* **5** 91–5

Jordana J, Gasulla M and Pallàs-Areny R 2001 Electrical resistance tomography to detect leaks from buried pipes *Meas. Sci. Technol.* **12** 1061–8

Kantartzis P, Abdi M and Liatsis P 2013 Stimulation and measurement patterns versus prior information for fast 3D EIT: a breast screening case study *Signal Process.* **93** 2838–50 Signal and Image Processing Techniques for Detection of Breast Diseases

Karimi A, Taghizadeh L and Heitzinger C 2021 Optimal Bayesian experimental design for electrical impedance tomography in medical imaging *Comput. Meth. Appl. Mech. Eng.* **373** 113489

Kauppinen P, Hyttinen J and Malmivuo J 2006 Sensitivity distribution visualizations of impedance tomography measurement strategies *Int. J. Bioelectromagn.* **8** 63–71 https://ijbem.org/volume8/number1/63-71.pdf

Lakshminarayanan V and Fleck A 2011 Zernike polynomials: a guide *J. Mod. Opt.* **58** 1678–1678

Lipponen A, Seppanen A and Kaipio J P 2013 Electrical impedance tomography imaging with reduced-order model based on proper orthogonal decomposition *J. Electron. Imaging* **22** 1–16

Liu K, Wu Y, Wang S, Wang H, Chen H, Chen B and Yao J 2020 Artificial sensitive skin for robotics based on electrical impedance tomography *Adv. Intell. Syst.* **2** 1900161

Ma G, Hao Z, Wu X and Wang X 2020 An optimal electrical impedance tomography drive pattern for human-computer interaction applications *IEEE Trans. Biomed. Circuits Syst.* **14** 402–11

Menke W 2012 *Geophysical Data Analysis: Discrete Inverse Theory* 3rd edn (Academic Press)

Paldanius A, Dekdouk B, Toivanen J, Kolehmainen V and Hyttinen J 2022 Sensitivity analysis highlights the importance of accurate head models for electrical impedance tomography monitoring of intracerebral hemorrhagic stroke *IEEE Trans. Biomed. Eng.* **69** 1491–501

Polydorides N and Lionheart W R 2002 A matlab toolkit for three-dimensional electrical impedance tomography: a contribution to the electrical impedance and diffuse optical reconstruction software project *Meas. Sci. Technol.* **13** 1871–83

Polydorides N and McCann H 2002 Electrode configurations for improved spatial resolution in electrical impedance tomography *Meas. Sci. Technol.* **13** 1862–70

Press W H, Teukolsky S A, Vetterling W T and Flannery B P 2007 *Numerical Recipes 3rd Edition: The Art of Scientific Computing* 3rd edn (Cambridge University Press)

Proença M, Rapin M, Braun F, Solà J, Lemay M and Thiran J P 2014 Cardiac output measured by electrical impedance tomography *2014 IEEE Biomedical Circuits and Systems Conf. (BioCAS)2014 IEEE Biomedical Circuits and Systems Conf. (BioCAS) Proc.* (IEEE) pp 236–9

Putensen C, Hentze B, Muenster S and Muders T 2019 Electrical impedance tomography for cardio-pulmonary monitoring *J. Clin. Med.* **8** 1176

Ragheb A, Geddes L, Bourland J and Tacker W 1992 Tetrapolar electrode system for measuring physiological events by impedance *Med. Biol. Eng. Comput.* **30** 117–117

Rao A, Teng Y C, Schaef C, Murphy E K, Arshad S, Halter R J and Odame K 2018 An analog front end asic for cardiac electrical impedance tomography *IEEE Trans. Biomed. Circuits Syst.* **12** 729–38

Smyl D and Liu D 2020 Optimizing electrode positions in 2D electrical impedance tomography using deep learning *IEEE Trans. Instrum. Meas.* **69** 6030–44

Tang M, Wang W, Wheeler J, McCormick M and Dong X 2002 The number of electrodes and basis functions in EIT image reconstruction *Physiol. Meas.* **23** 129–40

Tapp H, Peyton A, Kemsley E and Wilson R 2003 Chemical engineering applications of electrical process tomography *Sensors Actuators* B **92** 17–24

Tarantola A 2005 *Inverse Problem Theory and Methods for Model Parameter Estimation* (Society for Industrial and Applied Mathematics)

Thürk F, Elenkov M, Waldmann A D, Böhme S, Braun C, Adler A and Kaniusas E 2019 Influence of reconstruction settings in electrical impedance tomography on figures of merit and physiological parameters *Physiol. Meas.* **40** 094003

Van der Pauw L 1958 A method of measuring specific resitivity and Hall effect of discs of arbitrary shape *Philips Res. Rep.* **13** 1–9

Vauhkonen M, Kaipio J, Somersalo E and Karjalainen P 1997 Electrical impedance tomography with basis constraints *Inverse Prob.* **13** 523–30

Vauhkonen M, Lionheart W R B, Heikkinen L M, Vauhkonen P J and Kaipio J P 2001 A MATLAB package for the EIDORS project to reconstruct two-dimensional EIT images *Physiol. Meas.* **22** 107–11

Wagenaar J and Adler A 2016 Electrical impedance tomography in 3D using two electrode planes: characterization and evaluation *Physiol. Meas.* **37** 922–37

Williamson D P and Shmoys D B 2011 *The Design of Approximation Algorithms* (Cambridge University Press)

Yan W, Hong S and Chaoshi R 2006 Optimum design of electrode structure and parameters in electrical impedance tomography *Physiol. Meas.* **27** 291–306

Yasin M, Böhm S, Gaggero P O and Adler A 2011 Evaluation of EIT system performance *Physiol. Meas.* **32** 851–65

Yorkey T J, Webster J G and Tompkins W J 1987 Comparing reconstruction algorithms for electrical impedance tomography *IEEE Trans. Biomed. Eng.* **BME-34** 843–52

Zhang Y, Xiao R and Harrison C 2016 Advancing hand gesture recognition with high resolution electrical impedance tomography *29th Annual Symp. on User Interface Software and TechnologyProc. of the 29th Annual Symp. on User Interface Software and Technology* (https://doi.org/10.1145/2984511.2984574)

Zlochiver S, Freimark D, Arad M, Adunsky A and Abboud S 2006 Parametric EIT for monitoring cardiac stroke volume *Physiol. Meas.* **27** S139–46